Supplementary Information

Polaron absorption in aligned conjugated polymer films: Breakdown of the adiabatic treatment and going beyond the conventional mid-gap state model

Contents

S1 Methods **1**
S1.1 Polymer Synthesis . . . 1
S1.2 Polymer film alignment . . . 2
S1.3 X-ray scattering pole figure construction . . . 2
S1.4 Electron diffraction . . . 3
S1.5 UV-Vis Absorption . . . 3
S1.6 Charge modulation spectroscopy . . . 3
S1.7 Fourier Transform Infrared Spectroscopy . . . 3

S2 Supplemental Notes **4**
S2.1 Supplemental Note 1: Differential Transmission Measurements . . . 4
S2.2 Supplemental Note 2: Pole Figure Construction . . . 4
S2.3 Supplemental Note 3: Crystallite out-of-plane orientation effects on inter-chain absorption . . . 6
S2.4 Supplemental Note 4: Polaron Absorption Modeling . . . 10
S2.5 Supplemental Note 5: Charge density estimates . . . 12

S3 Supplemental Figures and Tables **13**
S3.1 Relative Spectral Weight: . . . 13
S3.2 UV-Vis and Exciton Absorption Features: . . . 13
S3.3 X-ray characterization of polymer thin films: . . . 14
S3.4 Polarized FTIR absorbance: . . . 15
S3.5 Component fits to Polarized CMS Data: . . . 16
S3.6 Effect of vibronic coupling on polaron absorption spectra . . . 17

S1 Methods

S1.1 Polymer Synthesis

Materials 2-bromo-3-hexyl-5-iodothiophene was purchased from TCI America, filtered through a silica plug in hexanes, and dried prior to use. All other chemicals were purchased from Sigma Aldrich and used without further processing.

Bromo(2-methylphenyl)bis(triphenylphosphine)nickel(II) Nickel(II) Bromide (2.19 g, 10 mmol) and triphenylphosphine (5.25 g, 20 mmol) were added to a 3-neck flask with an attached condenser and dried under vacuum for 30 minutes. After drying, 15 mL anhydrous THF was added. The flask was brought to 70°C and the mixture was refluxed for 2 h. Mg turnings (0.29 g, 12 mmol) were added to a Schlenk flask and flame dried under vacuum. After drying, 1 M 2-bromotoluene in anhydrous THF (10 mL, 10 mmol) was added dropwise to the Schlenk flask. The mixture was stirred for 1 h under darkness. The 3-neck flask was allowed to cool to room temperature and the Grignard solution was injected into it. The mixture was stirred for 20 minutes at room temperature and then quenched by pouring into

methanol. The product was vacuum filtered with fine glass frit, washed with methanol, and dried under vacuum. ^{13}P NMR Shifts: δ 21.97 (s, 2P)

Poly(3-hexylthiophene-2,5-diyl) (regioregular) 1,3-bis(diphenylphosphino)propane (41.25 mg, 0.05 mmol) and bromo-(2-methylphenyl)bis(triphenylphosphine)nickel(II) (37.72 mg, 0.1 mmol) were added to a Schlenk flask, and dried under vacuum for 30 min. After drying, anhydrous THF (2 mL) was added, and the mixture was stirred for 2 h. 2-bromo-3-hexyl-5-iodothiophene (1.45 mL, 6.6 mmol) was added to a Schlenk flask and degassed under vacuum for 30 min. Anhydrous THF (66 mL) was added to the Schlenk flask, the flask was placed in an ice bath and 1.85 M isopropylmagnesium chloride in THF (3.24 mL, 6 mmol) was added dropwise over 30 min. Following addition, the flask was returned to room temperature, and stirred for 1 h under darkness. The catalyst mixture was injected rapidly to the monomer flask to start the polymerization. Immediately after injection, the flask was placed in an oil bath at 45°C to prevent precipitation. The polymerization proceeded for 2 h. The polymerization was quenched with the addition of HCl (3 mL, 5 M). The polymer was precipitated into methanol (1000 mL) and collected by vacuum filtration. The polymer was purified using Soxhlet extraction with methanol, acetone, and hexanes. The polymer was extracted from the thimble with chloroform, then precipitated into methanol and collected via vacuum filtration. The polymer was dried under vacuum. ^{1}H NMR spectra were obtained on a Bruker AV-500 spectrometer using $CDCl_3$ as solvent. Size exclusion chromatography (SEC) was performed using a Malvern Viscotek TDA 305 SEC with a UV and RI detector. Samples were run using THF as the eluent at a flow rate of 1 mL min^{-1}. The concentration of the polymer was 0.5 mg mL^{-1}. The molecular weight distribution is determined by SEC, and the M_n is obtained by NMR end-group analysis. Regioregularity was determined by comparing the ratio of integrations of the head-to-tail couplings against tail-to-tail and head-to-head couplings; these showed the polymers to be $>99\%$ Regioregular within the resolution of the NMR. ^{1}H NMR Shifts: δ 7.43 (m, 2H), 7.24 (m, 2H), 6.98 (s, 1H), 2.80 (t, 2H (2H between the peaks at 2.8 and 2.61), J = 7.7 Hz), 2.61 (t, 2H (2H between the peaks at 2.8 and 2.61), J = 7.6), 2.49 (s, 3H), 1.71 (quint, 2H, J = 7.6 Hz), 1.48-1.38 (m, 2H), 1.37-1.30 (m, 4H), 0.91 (t, 3H, J = 7.2 Hz).

S1.2 Polymer film alignment

Poly(3-hexylthiophene-2,5-diyl) (P3HT) films were prepared by doctor blading a 10 mg ml^{-1} solution in ortho-dichlorobenzene (ODCB) at 150°C on either 1) glass substrates coated with a thin film of NaPSS or 2) silicon substrates with either a 150 nm thermal oxide SiO_2 layer or native oxide SiO_2 layer. Glass substrates consisted of microscope slides that were cleaned by sonication (15 min each) in acetone, ethanol, diluted aqueous solution of hellmanex and three rinsing steps in distilled water. A 10 mg ml^{-1} solution of Sodium poly(styrene sulfonate) (NaPSS, Aldrich) was spin-coated (3000 RPM) onto the clean glass substrates and used as a sacrificial layer to recover the P3HT films by floating the films on TEM copper grids. Silicon substrates were cleaned and prepared in an analogous manner, but there was no layer of NaPSS on these substrates.

Thin film alignment on all substrates was achieved by an elevated temperature shearing method described previously [1]. Briefly, shearing is accomplished by rubbing the top surface of the polymer film, deposited on either glass with sacrificial NaPSS or silicon substrates, with a microfiber cloth at elevated temperature. Rubbing was performed using a home-made rubbing machine under nitrogen atmosphere in a Plaslab glovebox. The rubbing machine consists of a rotating cylinder covered with a microfiber cloth (350 RPM) applied at 2-3 bar pressure on the P3HT film mounted on a translating hot stage (1mm s^{-1}). The temperature of the hot stage is the rubbing temperature, set at 230°C. Film thicknesses were typically $\sim$175 nm.

S1.3 X-ray scattering pole figure construction

Samples for X-ray scattering experiments were prepared via the shear alignment method described in Section S1.2 with thin films on silicon substrates with a native oxide layer. Grazing incidence wide-angle X-ray scattering (GIWAXS) was performed at Beamline 11-3 at Stanford Synchrotron Radiation Lightsource (SSRL) using an incident energy of 12.7 keV and Rayonix MAR-225 flat area detector. An incidence angle of 0.1° was used, as this angle allows the X-ray to penetrate the depth of the polymer thin film while being below the critical angle of the silicon substrate. Sample to detector distance and beam center position were calibrated using a polycrystalline LaB_6 standard. Raw data was corrected for geometric distortions introduced by the flat area detector using Nika 1D SAXS [2] and WAXStools software packages in Igor Pro [3]. Lineout scattering data is shown in terms of the scattering vector Q, where $Q = \frac{4\pi}{\lambda}\sin(\theta_B)$, λ is the incident X-ray wavelength, and θ_B is the Bragg scattering angle. Local specular X-ray scattering

of the samples was performed at Beamline 11-3 also by placing the angle of incidence equal to the approximate Bragg scattering angle for the (100) lamellar peak as found from GIWAXS. The sample angle of incidence was then rocked such that the full Bragg peak was captured. Resolution limited rocking scans were performed at Beamline 2-1 at SSRL with an incident energy of 12.7 keV with a Pilatus100K detector. Two pairs of slits were used to provide beam collimation with a slits size of 1mm.

S1.4 Electron diffraction

Oriented P3HT films prepared on glass slides with a sacrificial NaPSS layer as described in Section S1.2 were coated with a thin amorphous carbon film ($<$ 2 nm thickness) using an Edwards Auto306 evaporator. The oriented P3HT films were floated on distilled water and recovered on TEM copper grids. A CM12 Philips microscope (120 kV) equipped with a MVIII (Soft Imaging System) camera was used for bright field and electron diffraction (ED) analysis. Low dose conditions were used to avoid beam damage of the samples. Calibration of the ED patterns was made thanks to oriented poly(tetrafluoroethylene) substrates prepared by friction transfer.

S1.5 UV-Vis Absorption

A Varian Cary 5000 spectrometer with polarized incident light (spectral resolution of 1 nm) was used to probe the P3HT film orientation. The light polarization angle is measured with respect to the rubbing direction (0° corresponds to the light polarization POL$\|$R and 90° to the light polarization POL$\perp$R).

S1.6 Charge modulation spectroscopy

CMS device preparation

Oriented P3HT thins films for CMS devices were fabricated as described in Section S1.2 on double-side polished n-type silicon substrates ($\rho_{\text{substrate}}$ = 1-10 Ω-cm) with a thermally grown 150nm SiO_2 dielectric layer. To generate the contacts necessary for carrier injection in CMS, a 15 nm semi-transparent gold contact was evaporated onto the polymer surface, and a 75 nm silver contact was evaporated onto a region of exposed silicon where the SiO_2 dielectric layer was scratched through using a diamond scribe to form the device gate contact.

CMS Measurement

Completed CMS devices were then loaded into a home-built nitrogen chamber with KBr infrared transparent windows to perform the necessary spectroscopy measurements. It should be emphasized that all sample preparation and testing steps were performed in dry nitrogen environments (dew point $\leq$ 100^{o}F, O_2 $\leq$ 0.5 ppm). The CMS measurement was performed by biasing CMS devices to V_G = -30V in accumulation and V_G = +10V in depletion, where V_G is the gate bias applied to the silicon substrate. This gives an areal charge density of $\rho_{\text{areal}} = C_{\text{SiO2}} \times V_G \times e^{-1} = 2.3 \times 10^{-8}$[F cm^{-2}] $\times$ 30 [V] $\times e^{-1} = 4.31 \times 10^{12}$ [cm^{-2}]. Details on charge density estimates are give in Section S2.5. The differential infrared spectrum ($\frac{\Delta T}{T}$) were accumulated for at least 12,000 individual spectral averages until average ΔT changes were less than 10^{-5} using a Nicolet iS50R Fourier Transform IR (FT-IR) spectrometer. Details of FT-IR operation and data processing are given in Section S1.7. A Keithley K2400 was used to apply the gate biases. Device biasing and spectral acquisition were controlled with a home-built LabView code. Incident light polarization was accomplished with a wire grid ZnSe polarizer, with an alignment accuracy to the polymer thin film alignment direction of θ $\sim$0.5°. Data was collected in the spectral range of $\tilde{\nu}$ = 600-6000 [cm^{-1}] ($\sim$1.7-16.7 μm).

S1.7 Fourier Transform Infrared Spectroscopy

Oriented P3HT thins films for mid-IR absorbance measurements were fabricated as described in Section S1.2 on double-side polished n-type silicon substrates ($\rho_{\text{substrate}}$ = 1-10 Ω-cm) with a thermally grown 150nm SiO_2 dielectric layer. Thin film mid-IR absorbance spectra were collected using a Nicolet iS50R Fourier Transform Infrared (FTIR) spectrometer. As in the CMS experiments, incident light polarization was accomplished with a wire grid ZnSe polarizer. IR absorbance measurements and CMS measurements were performed with a DLaTGS detector. Two levels of interferrogram zero-filling were used. Norton-Beer Strong apodization was used [4] and the Mertz phase-correction procedure was employed [5] for interferrogram data processing.

S2 Supplemental Notes

S2.1 Supplemental Note 1: Differential Transmission Measurements

Differential transmission (ΔT) is reported as the change in transmission of a sample going from higher charge density (T_+) to a lower charge density (T_-), normalized by the neutral sample transmission (T_0), and can be shown to be approximately equal to the negative change in sample absorption coefficient ($\Delta\alpha$) multiplied by the absorbing layer thickness (D). In this work, the absorbing layer thickness D was kept at 1 nm as an estimate for the charge accumulation layer in CMS devices. All calculations are performed in terms of wavenumber, $\tilde{\nu}$ [cm^{-1}].

$$\frac{\Delta T(\tilde{\nu})}{T_0(\tilde{\nu})} = \frac{T_+(\tilde{\nu}) - T_-(\tilde{\nu})}{T_0(\tilde{\nu})} \approx -\Delta\alpha(\tilde{\nu})D \tag{S1}$$

Based on this, it is standard to report differential transmission data as $-\frac{\Delta T(\tilde{\nu})}{T_0(\tilde{\nu})} = \Delta\alpha(\tilde{\nu})D$. Optical absorption cross sections, $\sigma(\tilde{\nu})$, can be related to the differential transmission signal via:

$$\frac{\Delta T(\tilde{\nu})}{T_0(\tilde{\nu})} = -C_{areal}\, e^{-1}\, \Delta V \sigma(\tilde{\nu}) \tag{S2}$$

where, C_{areal} is the CMS gate oxide capacitance of a 150 nm layer of SiO_2, ΔV is the gate voltage modulation, and e is the elementary charge.
Spectral weights ($\Theta^{\text{abs}_i}_{\text{inter}}$ or $\Theta^{\text{abs}_i}_{\text{intra}}$) for a given absorption peak, abs_i, are computed by integration of the differential transmission data of absorption peak abs_i over its relevant spectral range:

$$\Theta^{\text{abs}_i}_{\text{inter or intra}} = \int_{\text{abs}_i} \left(\frac{\Delta T(\tilde{\nu})}{T_0(\tilde{\nu})}\right) d\tilde{\nu} = \int_{\text{abs}_i} \big(\Delta\alpha(\tilde{\nu})D\big) d\tilde{\nu} \tag{S3}$$

S2.2 Supplemental Note 2: Pole Figure Construction

The out-of-plane crystallite orientation, $I(\chi)$, was quantified by constructing a lamellar, (100) plane, pole figure according to methods outlined in Refs. [6] and [7]. Briefly, 3 separate synchrotron based X-ray scattering techniques are needed to construct a full pole figure: 1) a grazing incidence X-ray scattering scan with a 2D area detector to measure $I(\chi)$ from $|\chi|$=90° to $|\chi|$=2°, 2) a local specular X-ray scattering scan where X-ray scattering is measured at the relevant Bragg angle, θ_b, for the lamellar (100) plane ($\theta_b = 1.8°$) to measure $I(\chi)$ from χ=−3° to χ=3°, filling in the "missing wedge" of data that arises from inaccessible scattering geometries associated with grazing incidence scans and flat area detectors, and 3) a resolution-limited rocking scan conducted with a high resolution point detector to measure intensity within $\sim$0.1° of χ=0°.

This pole figure in Figure S1 yields X-ray scattering intensity of as a function of crystallite out-of-plane orientation angle (χ, the tilt of the a-axis relative to the substrate normal, as defined in Figure 2 of the main text). Because the films employed in this study are not in-plane isotropic (i.e. films are not fiber-textured), two different film orientations relative to the incident X-ray beam were needed to quantify out-of-plane crystallite orientation as shown in Figure S2. For the grazing incidence and local specular scans, the thin film was oriented such that the nominal polymer alignment direction was oriented in the direction of the incident X-ray wavevector (k_0) such that the out-of-plane crystallite orientation could be measured on a 2D area detector. For the resolution-limited rocking scan, the thin film was oriented with the nominal polymer alignment direction perpendicular to the incident X-ray wavevector. This scan uses a point detector and allows the measurement of crystallite out-of-plane orientation within $\chi\sim$0.1° of the substrate normal. The film is oriented perpendicular to the incident X-ray wavevector in this case, because the relevant out-of-plane orientation of interest for this work is the orientation around the nominal polymer alignment direction.

In this work, the same polymer film was used for all X-ray scattering experiments. Scattered X-ray intensity as a function of χ, $I(\chi)$, for the (100) lamellar plane is given by Equation S4.

$$I(\chi) = \alpha_{beam}\, N(\chi)\, I_0\, |F_{100}|^2 \tag{S4}$$

where α_{beam} captures properties of the X-ray beam (e.g. polarization, Lorentz factors, etc.), $N(\chi)$ is the number of diffracting unit cells with an orientation χ, I_0 is the incident X-ray beam intensity, and F_{100} is the (100) lamellar

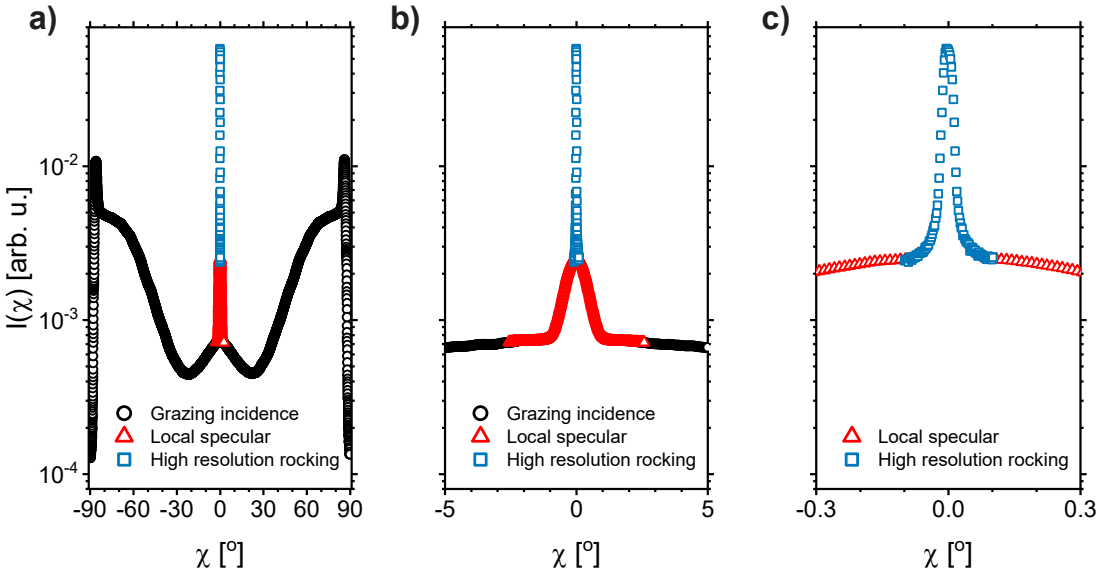

Figure S1: **a)** Lamellar (100) pole figure of aligned P3HT thin films showing the stitched spectra from three separate X-ray scattering experiments. **b)** A more detailed pole figure view from χ=$-5°$ to χ=5° showing the stitching of a local specular X-ray scattering scan and **c)** a more detailed pole figure view from χ=$-0.3°$ to χ=0.3° showing the resolution-limited rocking scan stitch with the local specular scan.

plane structure factor. In this work, all X-ray scattering data was normalized by I_0 and backgrounds were removed to normalize each scan by α_{beam}. This results in Equation S5 where the reported $I(\chi)$ depends only on the number of diffracting unit cells and the (100) structure factor.

$$I(\chi) = N(\chi)\ |F_{100}|^2 \tag{S5}$$

As outlined in Equations S29 and S30 in Section S2.3, the absolute value of $I(\chi)$ is not of great importance to this work since the spectral adjustments shown in Figure 4 of the main text depend only on the relative weights of the intra-chain and inter-chain absorption components. Therefore, we can still use $I(\chi)$ as a proxy for $N(\chi)$ even though the (100) structure factor is not known. With this result, we can use the measured $I(\chi)$ reported in Figure 3 of the main text as directly proportional to the out-of-plane orientation distribution of crystallites.

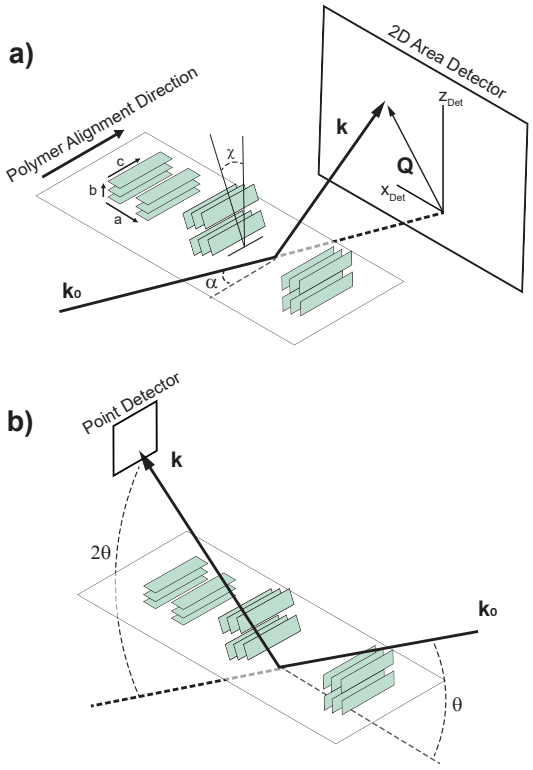

Figure S2: Schematic of polymer thin film orientation relative to the incident X-ray wavevector for **a)** grazing incidence and local specular X-ray scattering measurements and **b)** resolution-limited rocking scans. Relevant polymer stacking axes as defined in Figure 2 of the main text are shown. The scattered wavevector k is shown along along with the scattering vector Q. α represents the substrate tilt relative to the incident X-ray wavevector for grazing incidence and local specular scans, and θ represents the substrate tilt relative to the incident X-ray wavevector for the resolution limited scan.

S2.3 Supplemental Note 3: Crystallite out-of-plane orientation effects on inter-chain absorption

Geometry definitions

Polymer aggregates are defined by two orientation distributions: the in-plane orientation, $F(\phi)$, defined by the chain axis of the crystallite with respect to an arbitrary direction (here the X-direction), and the tilt orientation, $I(\beta)$, of the crystallite π-conjugated backbone with respect to the substrate. These relevant orientations are shown in Figure S3. Each crystallite then has vectors that are functions of ϕ and β associated with infrared-active transition dipoles that point along the chain axis, $\boldsymbol{\mu}_{\parallel}(\phi,\beta) = \mu_{\parallel}\,\hat{\boldsymbol{\mu}}_{\parallel}(\phi,\beta)$ and orthogonal to this along the π-stacking direction, $\boldsymbol{\mu}_{\perp}(\phi,\beta) = \mu_{\perp}\,\hat{\boldsymbol{\mu}}_{\perp}(\phi,\beta)$, where $\hat{\boldsymbol{\mu}}_{\parallel}(\phi,\beta)$ is the unit vector pointing along the direction of $\boldsymbol{\mu}_{\parallel}(\phi,\beta)$ and $\hat{\boldsymbol{\mu}}_{\perp}(\phi,\beta)$ is the unit vector pointing along the direction $\boldsymbol{\mu}_{\perp}(\phi,\beta)$. $\hat{\boldsymbol{\mu}}_{\parallel}(\phi,\beta)$ and $\hat{\boldsymbol{\mu}}_{\perp}(\phi,\beta)$ are both defined by rotations of starting unit vectors by ϕ about the Z-axis and β about the X-axis. In the event of no rotation where $\phi = 0°$ and $\beta = 0°$:

$$\hat{\boldsymbol{\mu}}_{\parallel}(\phi=0,\beta=0) = \begin{bmatrix}1\\0\\0\end{bmatrix} \tag{S6}$$

and

$$\hat{\boldsymbol{\mu}}_{\perp}(\phi=0,\beta=0) = \begin{bmatrix}0\\0\\1\end{bmatrix} \tag{S7}$$

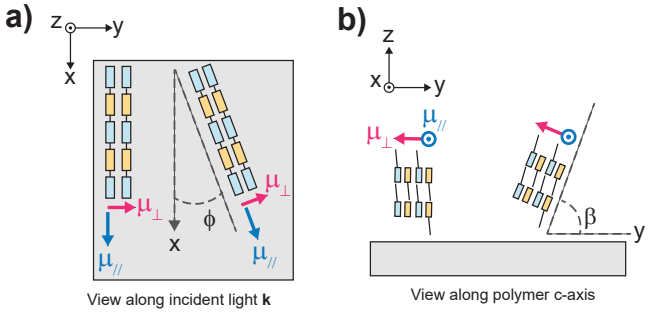

Figure S3: Relevant geometric definitions for polymer inter- and intra-chain absorption calculations. **a)** View along the incident light wavevector, **k** of aligned polymer films with relevant axes labeled. The polymer backbone (c-axis) is defined relative to the substrate X-direction by the angle ϕ. **b)** View along the polymer c-axis of aligned polymer films. Polymer π-overlap orientation and the corresponding intra- and inter-chain TDMs are defined by the angle β from the substrate plane (the X-Y plane). Note, $\beta = 90° - \chi$, where χ is the angle between the polymer lamellar stacking axis (the a-axis) and the substrate normal, as defined in Figure 2 of the main text. Note, in the schematic shown in panel b, the polymer chain axis is oriented perfectly along the X-direction, but this need not be true as we include the possibility that there is some in-plane orientation distribution about the X-direction.

Rotations of $\hat{\boldsymbol{\mu}}_{\parallel}(0,0)$ and $\hat{\boldsymbol{\mu}_{\perp}}(0,0)$ to arbitrary ϕ and β are accomplished by applying the rotation matrix $R_x(\beta)$ about the X-axis and $R_z(\phi)$ about the Z-axis where:

$$R_x(\beta) = \begin{bmatrix} 1 & 0 & 0 \\ 0 & \cos(\beta) & -\sin(\beta) \\ 0 & \sin(\beta) & \cos(\beta) \end{bmatrix} \tag{S8}$$

and

$$R_z(\phi) = \begin{bmatrix} \cos(\phi) & -\sin(\phi) & 0 \\ \sin(\phi) & \cos(\phi) & 0 \\ 0 & 0 & 1 \end{bmatrix} \tag{S9}$$

Applying $R_x(\beta)$ and $R_z(\phi)$ to $\hat{\boldsymbol{\mu}}_{\parallel}(0,0)$ and $\hat{\boldsymbol{\mu}_{\perp}}(0,0)$, $\hat{\boldsymbol{\mu}}_{\parallel}(\phi,\beta)$ and $\hat{\boldsymbol{\mu}_{\perp}}(\phi,\beta)$ are given in Equations S10 and S11 respectively.

$$\hat{\boldsymbol{\mu}}_{\parallel}(\phi,\beta) = R_z(\phi)R_x(\beta)\begin{bmatrix} 1 \\ 0 \\ 0 \end{bmatrix} = \begin{bmatrix} \cos(\phi) \\ \sin(\phi) \\ 0 \end{bmatrix} \tag{S10}$$

$$\hat{\boldsymbol{\mu}_{\perp}}(\phi,\beta) = R_z(\phi)R_x(\beta)\begin{bmatrix} 0 \\ 0 \\ 1 \end{bmatrix} = \begin{bmatrix} \sin(\phi)\sin(\beta) \\ -\cos(\phi)\sin(\beta) \\ \cos(\beta) \end{bmatrix} \tag{S11}$$

Where $\hat{\boldsymbol{\mu}}_{\parallel}(\phi,\beta) \cdot \hat{\boldsymbol{\mu}_{\perp}}(\phi,\beta) = 0$ satisfy the requirement that these two vectors are orthogonal.

Relation of absorption coefficient to crystallite orientation

The absorption coefficient, $\alpha(\hbar\omega,\phi,\beta)$, can be written as proportional to the square of the momentum matrix elements for photon absorption/emission processes such that the polarized components of absorption in the intra-chain direction, $\alpha_{\parallel}(\hbar\omega,\phi,\beta)$, and inter-chain direction, $\alpha_{\perp}(\hbar\omega,\phi,\beta)$ can be written in terms of the perturbing electric field, $\boldsymbol{E} = E_0\hat{\boldsymbol{E}}$, and the transition dipole moments of the intra-chain and inter-chain absorption processes such that:

$$\alpha_{\parallel}(\hbar\omega,\phi,\beta) \propto E_0^2\,\mu_{\parallel}^2\,|\hat{\boldsymbol{E}}\cdot\hat{\boldsymbol{\mu}}_{\parallel}(\phi,\beta)|^2 \tag{S12}$$

and

$$\alpha_{\perp}(\hbar\omega, \phi, \beta) \propto E_0^2 \; \mu_{\perp}^2 \; |\hat{\boldsymbol{E}} \cdot \hat{\boldsymbol{\mu}_{\perp}}(\phi, \beta)|^2 \tag{S13}$$

The perturbing electric field unit vector, $\hat{\boldsymbol{E}}$, can be defined relative to the X-direction of the polymer substrate by applying rotation matrices to a unit vector pointing along the X-direction. In this case, the polymer substrate can effectively have two defining angles relative to the electric field: the orientation of the substrate X-direction relative to the electric field, θ, and the orientation of the substrate normal to the wavevector of the electric field, γ. In this work, we maintained the substrate X-Y plane normal to the incoming electric field wavevector. This results in $\hat{\boldsymbol{E}}(\theta)$ defined as:

$$\hat{\boldsymbol{E}}(\theta, \gamma) = R_z(\theta) \begin{bmatrix} 1 \\ 0 \\ 0 \end{bmatrix} = \begin{bmatrix} \cos(\theta) & -\sin(\theta) & 0 \\ \sin(\theta) & \cos(\theta) & 0 \\ 0 & 0 & 1 \end{bmatrix} \begin{bmatrix} 1 \\ 0 \\ 0 \end{bmatrix} = \begin{bmatrix} \cos(\theta) \\ \sin(\theta) \\ 0 \end{bmatrix} \tag{S14}$$

With $\hat{\boldsymbol{\mu}_{\parallel}}\phi, \beta)$, $\hat{\boldsymbol{\mu}_{\perp}}\phi, \beta)$, and $\hat{\boldsymbol{E}}(\theta, \gamma)$ defined, Equations S12 and S13 can be evaluated fully such that the polarized absorption coefficients are functions of $\hbar\omega$, ϕ, β, and θ. Equations S15 and S16 effectively give the absorption coefficient for a single polymer crystallite oriented with its chain axis at an angle ϕ relative to the substrate X-direction and its lamellar-stacking axis at an angle β relative to the substrate surface. In Equations S15 and S16, the incident perturbing electric field is oriented by an angle θ relative to the X-direction and with its wavevector at an angle γ relative to the substrate normal. To account for the different amounts of crystallites at specific ϕ and α orientations, the distribution functions for in-plane orientation, $F(\phi)$, and tilt orientation, $I(\beta)$, are introduced.

$$\begin{gathered} \alpha_{\parallel}(\hbar\omega, \phi, \beta, \theta) \propto E_0^2 \; \mu_{\parallel}^2 \; \left(\hat{\boldsymbol{E}}(\theta) \cdot \hat{\boldsymbol{\mu}_{\parallel}}(\phi, \beta) \; F(\phi) \; I(\beta)\right)^2 = \\ E_0^2 \; \mu_{\parallel}^2 \left(\begin{bmatrix} \cos(\theta) \\ \sin(\theta) \\ 0 \end{bmatrix} \cdot \begin{bmatrix} \cos(\phi) \\ \sin(\theta) \\ 0 \end{bmatrix} \; F(\phi) \; I(\beta) \right)^2 = \\ E_0^2 \; \mu_{\parallel}^2 \left(\left[\cos(\theta) \; \cos(\phi) + \sin(\phi) \; \sin(\theta) \right] F(\phi) \; I(\beta) \right)^2 \end{gathered} \tag{S15}$$

$$\begin{gathered} \alpha_{\perp}(\hbar\omega, \phi, \beta, \theta) \propto E_0^2 \; \mu_{\perp}^2 \; \left(\hat{\boldsymbol{E}}(\theta) \cdot \hat{\boldsymbol{\mu}_{\perp}}(\phi, \beta) \; F(\phi) \; I(\beta)\right)^2 = \\ E_0^2 \; \mu_{\perp}^2 \left(\begin{bmatrix} \cos(\theta) \\ \sin(\theta) \\ 0 \end{bmatrix} \cdot \begin{bmatrix} \sin(\phi)\sin(\beta) \\ -\cos(\phi)\sin(\beta) \\ \cos(\beta) \end{bmatrix} \; F(\phi) \; I(\beta) \right)^2 = \\ E_0^2 \; \mu_{\perp}^2 \left(\left[\cos(\theta) \; \sin(\phi) \; \sin(\beta) - \cos(\phi) \; \sin(\theta) \; \sin(\beta) \right] F(\phi) \; I(\beta) \right)^2 \end{gathered} \tag{S16}$$

The spectroscopic measurements make no inherent discrimination of absorption based on the two relevant polymer orientation distribution functions, $F(\phi)$ and $I(\beta)$; these are experimentally determined distributions. Therefore, the absorption coefficients as a function of θ and $\hbar\omega$ only require integrations of the polymer orientation distribution functions over the relevant domains:

$$\alpha_{\parallel}(\hbar\omega, \theta) \propto E_0^2 \; \mu_{\parallel}^2 \left(\int_{\beta=0^{\circ}}^{\beta=180^{\circ}} \int_{\phi=-90^{\circ}}^{\phi=90^{\circ}} F(\phi) \; I(\beta) \left[\cos(\theta) \; \cos(\phi) + \sin(\phi) \; \sin(\theta) \right] d\phi \, d\beta \right)^2 \tag{S17}$$

$$\alpha_{\perp}(\hbar\omega, \theta) \propto E_0^2 \; \mu_{\perp}^2 \left(\int_{\beta=0^{\circ}}^{\beta=180^{\circ}} \int_{\phi=-90^{\circ}}^{\phi=90^{\circ}} F(\phi) \; I(\beta) \left[\cos(\theta) \; \sin(\phi) \; \sin(\beta) - \cos(\phi) \; \sin(\theta) \; \sin(\beta) \right] d\phi \, d\beta \right)^2 \tag{S18}$$

Based on the electron diffraction (Figure 3 of the main text) and the polarized IR absorbance (Figure S7), we take the polymer films to be well aligned to such a degree that $F(\phi)$ can be approximated by a delta function centered at $\phi = 0$ (that is, all polymer chains are oriented perfectly along the X-direction under this assumption). Using:

$$F(\phi) = \delta(\phi) \tag{S19}$$

The sifting property of the $\delta(\phi)$ effectively removes the ϕ dependence in Equations S17 and S18, resulting in:

$$\alpha_{\parallel}(\hbar\omega,\theta) \propto E_0^2\ \mu_{\parallel}^2\ \cos^2(\theta)\Big(\int_{\beta=0^\circ}^{\beta=180^\circ} I(\beta)\,d\beta\Big)^2 \tag{S20}$$

$$\alpha_{\perp}(\hbar\omega,\theta) \propto E_0^2\ \mu_{\perp}^2\ \sin^2(\theta)\Big(\int_{\beta=0^\circ}^{\beta=180^\circ} I(\beta)\ \sin(\beta)\,d\beta\Big)^2 \tag{S21}$$

Equations S20 and S21 now contain integrations that only involve $I(\beta)$, which is experimentally determinable from x-ray scattering pole figure construction (Figure 3 of main text). The x-ray scattering technique employed in this work is based on finding relative diffraction intensity for crystallites as a function of χ, which is defined relative to the substrate normal. To make equations S20 and S21 more amenable to the experimental x-ray scattering pole figure, a change of variables is introduced such that:

$$\chi = 90^\circ - \beta \tag{S22}$$

Incorporating this change of variable into equations S20 and S21 yields:

$$\begin{aligned}\alpha_{\parallel}(\hbar\omega,\theta) \propto E_0^2\ \mu_{\parallel}^2\ \cos^2(\theta)\Big(\int_{\chi=90^\circ}^{\chi=-90^\circ} I(\chi)\,(-d\chi)\Big)^2 = \\ E_0^2\ \mu_{\parallel}^2\ \cos^2(\theta)\Big(\int_{\chi=-90^\circ}^{\chi=90^\circ} I(\chi)\,(d\chi)\Big)^2\end{aligned} \tag{S23}$$

$$\begin{aligned}\alpha_{\perp}(\hbar\omega,\theta) \propto E_0^2\ \mu_{\perp}^2\ \sin^2(\theta)\Big(\int_{\beta=0^\circ}^{\beta=180^\circ} I(\beta)\ \sin(\beta)\,d\beta\Big)^2 = \\ E_0^2\ \mu_{\perp}^2\ \sin^2(\theta)\Big(\int_{\chi=90^\circ}^{\chi=-90^\circ} I(\chi)\ \sin(90^\circ-\chi)\,(-d\chi)\Big)^2 = \\ E_0^2\ \mu_{\perp}^2\ \sin^2(\theta)\Big(\int_{\chi=-90^\circ}^{\chi=90^\circ} I(\chi)\ \cos(\chi)\,(d\chi)\Big)^2\end{aligned} \tag{S24}$$

The integrals in equations S23 and S24 were evaluated using the experimentally generated $I(\chi)$ distribution. Defining:

$$\int_{\chi=-90^\circ}^{\chi=90^\circ} I(\chi)\,(d\chi) = P_f \tag{S25}$$

and

$$\int_{\chi=-90^\circ}^{\chi=90^\circ} I(\chi)\ \cos(\chi)\,(d\chi) = P_f' \tag{S26}$$

Scaling factor for experimental data

If the films used in this experiment were perfectly edge-on, such that $I(\chi) = \delta(\chi)$, then $P_f = P_f'$. Since this is not the case, we seek some way to compare the measured polarized polaron absorption components quantitatively. In equations S23 and S24, $\alpha_{\parallel}(\hbar\omega,\theta)$ and $\alpha_{\perp}(\hbar\omega,\theta)$ are the experimentally measured quantities from charge modulation spectroscopy. We can think of these quantities as proportional to the actual intra-molecular and inter-molecular polarized polaron absorption components (defined as $\alpha_{\parallel}^0(\hbar\omega) = E_0^2\ \mu_{\parallel}^2$ and $\alpha_{\perp}^0(\hbar\omega) = E_0^2\ \mu_{\perp}^2$ respectively), but weighted by the crystallite orientation factors of $\left(P_f\right)^2$ and $\left(P_f'\right)^2$, along with the geometric consideration of the incident light orientation. The relative intensity of these absorption components $\alpha_{\parallel}^0(\hbar\omega) = E_0^2\ \mu_{\parallel}^2$ and $\alpha_{\perp}^0(\hbar\omega) = E_0^2\ \mu_{\perp}^2$ are the goal of this work. Rewriting equations S23 and S24 as:

$$\alpha_{\parallel}(\hbar\omega,\theta) = \alpha_{\parallel}^0(\hbar\omega)\ \cos^2(\theta)\ \left(P_f\right)^2 \tag{S27}$$

and

$$\alpha_{\perp}(\hbar\omega,\theta) = \alpha_{\perp}^0(\hbar\omega)\ \sin^2(\theta)\ \left(P_f'\right)^2 \tag{S28}$$

Because the absolute values of $\alpha_{\parallel}^{0}(\hbar\omega)$ and $\alpha_{\perp}^{0}(\hbar\omega,\theta)$ are not of great importance to this work, we can arbitrarily divide both equations S27 and S28 by a factor of $\left(P_f\right)^2$. Performing this division, and then rearranging equations S27 and S28 to solve for $\alpha_{\parallel}^{0}(\hbar\omega,\theta)$ and $\alpha_{\perp}^{0}(\hbar\omega,\theta)$ respectively, we find:

$$\alpha_{\parallel}^{0}(\hbar\omega) = \frac{\alpha_{\parallel}(\hbar\omega,\theta)}{\cos^2(\theta)} \tag{S29}$$

and

$$\alpha_{\perp}^{0}(\hbar\omega) = \frac{\alpha_{\perp}(\hbar\omega,\theta)}{\sin^2(\theta)} \frac{\left(P_f\right)^2}{\left(P_f'\right)^2} = \frac{\alpha_{\perp}(\hbar\omega,\theta)}{\sin^2(\theta)} \times 2.45 \tag{S30}$$

In Equations S29 and S30, the $\cos^2(\theta)$ and $\sin^2(\theta)$ terms go to unity when the pure intrachain and pure interchain spectra are measured at incident light electric field orientations of $\theta = 0^\circ$ ($\cos^2(0^\circ) = 1$) and $\theta = 90^\circ$ ($\sin^2(90^\circ) = 1$) respectively. At these conditions of the incident light electric field, we are experimentally measuring the term $\alpha_{\parallel}(\hbar\omega)$ which is exactly equal to $\alpha_{\parallel}^{0}(\hbar\omega)$, and we are measuring the term $\alpha_{\perp}(\hbar\omega)$, which is exactly equal to $\frac{\alpha_{\perp}^{0}(\hbar\omega)}{2.45}$ as shown in Equation S30. By scaling the experimental interchain spectrum $\alpha_{\perp}(\hbar\omega)$ by a factor of 2.45, based on the experimental $I(\chi)$ distribution and the evaluated integrals shown in Equations S25 and S26 $\left(\frac{(P_f)^2}{(P_f')^2} = \frac{0.6103^2}{0.3895^2} = \frac{0.3725}{0.1517} = 2.45(5)\right)$ we yield the pure interchain absorption component of $\alpha_{\perp}^{0}(\hbar\omega)$, adjusted for the effects of crystallite out-of-plane orientation distribution. Intuitively, this scaling factor should be larger than unity, since it is the experimental interchain component that is expected to be weakened based on crystallite orientation effects. This factor large than unity of 2.45 adjusts the interchain component to that expected from a perfectly edge-on crystallite, where the crystallite orientation effects would not weaken the interchain absorption component.

With the pure components of intrachain and interchain polaron absorption quantified in the form of $\alpha_{\parallel}^{0}(\hbar\omega)$ and $\alpha_{\perp}^{0}(\hbar\omega)$, model fits based on our modified Holstein Hamiltonian (see Section S2.4) can then be performed to these pure absorption components as shown in the main text Figure 4a,b. Model fits to other incident light polarization angles can then be found based on Equations S27 and S28. The intrachain and interchain components at an arbitrary polarization, θ, are just the pure component fits to $\alpha_{\parallel}^{0}(\hbar\omega)$ and $\alpha_{\perp}^{0}(\hbar\omega)$ modified by a geometric term that adjusts intensity based on the incident light polarization ($\cos^2(\theta)$ for the intrachain components and $\sin^2(\theta)$ for the interchain components) and modified by another geometric term that adjust intensity based on crystallite out-of-plane orientation (P_f for the intrachain components or P_f' for the interchain components, defined in Equations S25 and S26).

S2.4 Supplemental Note 4: Polaron Absorption Modeling

The spectral simulations in Figure 4 of the main text are based on the Hamiltonian in Eq.(1) of the main text with the following parameters. For details see Refs. [8, 9]. The intrachain hopping integral t_{intra} is taken to be -0.4 eV while the interchain hopping integral is t_{inter} = -0.11 eV. The aromatic-quinoidal vibrational energy is $\hbar\omega_{vib}$ = 0.17 eV while the Huang-Rhys factor is unity (λ^2 = 1). To account for inhomogeneous broadening we assume a value of σ_{dis} = 0.3 eV for the standard deviation of the Gaussian distribution in Eq.(4) along the polymer axis. The simulated spectra in Figure 4 were obtained by averaging over 1000 configurations of disorder. The model parameters are summarized in Table S1.

Table S1: Polaron Absorption Fitting Parameters in This Work

Parameter	Parameter Value
Polymer Chains, N	4
Thiophenes per chain, M	10
t_{intra}	-0.40 [eV]
t_{inter}	-0.11 [eV]
σ_{dis}	0.30 [eV]
Γ_{homo}	0.03 [eV]
Huang-Rhys factor , λ^2	1

Polaron Wavefunction

Under the two-particle approximation, the single-hole basis set used to represent H in Eq. (1) of the main text is truncated to include only one- and two-particle states; in a single-particle state, denoted as $|m,n,\nu\rangle$, a hole resides on the m$^{\text{th}}$ thiophene unit of the n$^{\text{th}}$ chain with ν vibrational quanta in its *shifted* (S+) potential well. The remaining N×M – 1 units are in their vibrationless ground states (filled fragment HOMO with no vibrations in the S_0 well). In a two-particle state, denoted $|m,n,\nu;m',n',\nu'\rangle$, the unit at (m,n) contains the hole, with ν vibrational quanta in S+, while the unit at (m',n') is electronically neutral, with $\nu' > 0$ vibrational quanta in the unshifted S_0 potential. The remaining N×M – 2 units are in their vibrationless ground states. Within the multi-particle basis set, eigenstates of H in Eq. (1) can be written as Equation S31:

$$|\Psi_a\rangle = \sum_{m,n=1} \sum_{\tilde{\nu}=0,1,\ldots} c^{\alpha}_{m,n,\tilde{\nu}} |m,n,\tilde{\nu}\rangle + \sum_{m,n,\tilde{\nu}} \sum_{m',n',\nu'} c^{\alpha}_{m,n,\tilde{\nu};m',n',\nu'} |m,n,\tilde{\nu};m',n',\nu'\rangle \tag{S31}$$

The one- and two-particle expansion coefficients can be readily obtained numerically. Three- and higher particle states with three or more monomer excitations (electronic plus vibrational) can also be included, but their impact is negligible on the calculated infrared spectra for the vibronic coupling parameters used here.

Infrared Absorption and Hole Coherence

The polarized absorption spectrum, $A_j(\omega)$, for a disordered polymer π-stack is evaluated using Equation S32:

$$A_j(\omega) = \left\langle \sum_{ex} f_j^{ex}\, W_{LS}\big[\hbar\omega - \big(E_{ex} - E_G\big)\big] \right\rangle_c \tag{S32}$$

where the index $j(= x, y)$ indicates the polarization direction, with x lying along a polymer chain axis (the c-axis in Figure 2 of the main text) and y lying along the π-stacking interchain axis (the b-axis in Figure 2 of the main text). The sum in Equation S32 is over all the polaron excited states and $\langle ... \rangle$ represents an average over many site-energy disorder configurations. W_{LS} is the *homogeneous* line shape function, taken here to be a narrow Gaussian with a standard deviation Γ_{homo}= 0.03 eV, an order of magnitude smaller than the assumed inhomogeneous width, σ = 0.3 eV. The oscillator strength, f_j^{ex} in Equation S32 pertaining to the j-polarized transition from the polaron ground state, Ψ_G to the higher excited state, Ψ_{ex} is given by Equation S33:

$$f_j^{ex} = \frac{2m_e}{3e^2\hbar^2}\big(E_{ex} - E_G\big)\big|\langle\Psi_G|\hat{\boldsymbol{\mu}}_j|\Psi_{ex}\rangle\big|^2 \tag{S33}$$

where m_e is electron mass and E_{ex} and E_G are the excited and ground state energies, respectively, obtained via diagonalization of H and the dipole moment operator $\hat{\boldsymbol{\mu}}$ is given by Equation S34:

$$\hat{\boldsymbol{\mu}} = e\sum_{m,n} \boldsymbol{r}_{m,n}\, d^{\dagger}_{m,n} d_{m,n} \tag{S34}$$

where, $d^{\dagger}_{m,n}$ ($d_{m,n}$) are the Fermion raising (lowering) operators for a single hole. Here, we have approximated the P3HT π-stack as a square lattice such that $\boldsymbol{r}_{m,n}$ = $ma\hat{\boldsymbol{i}} + na\hat{\boldsymbol{j}}$ with both the nearest-neighbor interchain distance (a) as well as the nearest-neighbor thiophene-thiophene distance (a) approximated as a = 0.4 nm. $\hat{\boldsymbol{i}}$ and $\hat{\boldsymbol{j}}$ are unit vectors along the polymer backbone c-axis and interchain axis π-stacking b-axis, respectively.

In what follows, we also evaluate the two-dimensional coherence function, $\mathrm{C_p}(\boldsymbol{r})$, describing hole delocalization in the ground state by Equation S35 [9]:

$$\mathrm{C_p}(\boldsymbol{r}) = \left\langle \langle\Psi_G| \sum_{\boldsymbol{R}} d^{\dagger}_{\boldsymbol{R}} d_{\boldsymbol{R}+\boldsymbol{r}} |\Psi_G\rangle \right\rangle_c \tag{S35}$$

where $\boldsymbol{R} = (m,n) = m\hat{\boldsymbol{i}} + n\hat{\boldsymbol{j}}$ is a dimensionless position vector. When $\boldsymbol{r} = (0,0)$, the coherence function, $\mathrm{C_p}(\boldsymbol{r})$, reduces to unity since $\sum_{\boldsymbol{R}} d^{\dagger}_{\boldsymbol{R}} d_{\boldsymbol{R}+\boldsymbol{r}}$ is the number operator for the holes, and we assume only a single hole. The total number of coherently connected thiophene units, N_{coh}, is obtained from the coherence function by evaluating the sum in Equation S36:

$$N_{coh} = \sum_{\boldsymbol{r}} \big|\mathrm{C_p}(\boldsymbol{r})\big| \tag{S36}$$

To obtain the coherence number along the polymer chain direction, N_{intra}, one needs to restrict the sum in Equation S36 to position vectors $\boldsymbol{r}$ lying along the chain backbone c-axis. Similarly, N_{inter} is evaluated by restricting the sum to vectors lying along the interchain π-stacking b-axis. The coherence number either along the polymer chain direction or along the π-stacking b-axis can then be used to estimate the polaron coherence length (L_{intra} or L_{inter}) by either Equation S37 or S38:

$$L_{\text{intra}} = (N_{\text{intra}} - 1) \times \ d_{\text{intra}} \tag{S37}$$

$$L_{\text{inter}} = (N_{\text{inter}} - 1) \times \ d_{\text{inter}} \tag{S38}$$

where d_{intra} and d_{inter} are the monomer-to-monomer repeat distance ($\sim$ 0.38 nm in P3HT [10]) and π-stacking distance (0.378 nm shown in Section S3.3) respectively.

S2.5 Supplemental Note 5: Charge density estimates

CMS devices were biased such that the polymer-dielectric interface had an interfacial area charge density of $\rho_{\text{areal}} = 4.31 \times 10^{12}$ [cm^{-2}] as calculated based on the areal capacitance of a 150nm SiO_2 dielectric layer ($C_{\text{SiO2}} \approx 2.30 \times 10^{-8}$ [F cm^{-2}], Section S1.6). In the following derivation, the charge accumulation layer thickness (t_{accum}) will be assumed to be $\sim$1 [nm], which yields a volumetric charge density of $\rho_{\text{vol}} = 4.31 \times 10^{19}$ [cm^{-3}] [11, 12]. Taking the monomer mass of P3HT ($m_{\text{monomer}} = 165.8[\text{g mol}^{-1}]$) and density ($\text{density}_{\text{P3HT}} \approx 1.1[\text{g cm}^{-3}]$), the monomer volume density can be calculated by Equation S39.

$$\begin{aligned} \text{density}_{\text{monomer}} = \text{density}_{\text{P3HT}} \times m_{\text{monomer}}^{-1} \times N_A = \\ 1.1 \text{ [g cm}^{-3}] \times \left(165.8 \text{ [g mol}^{-1}]\right)^{-1} \times 6.0223 \times 10^{23} [\text{monomers mol}^{-1}] \approx \\ 4.0 \times 10^{21} \text{ [monomers cm}^{-3}] \end{aligned} \tag{S39}$$

Based on the monomer density calculated from Equation S39, the number of monomers per charge can be estimated by Equation S40:

$$\text{monomers per charge} = \frac{4.0 \times 10^{21} \text{ [monomers cm}^{-3}]}{4.31 \times 10^{19} \text{ [cm}^{-3}]} \approx 93 \text{ [monomers charge}^{-1}] \tag{S40}$$

S3 Supplemental Figures and Tables

S3.1 Relative Spectral Weight:

Table S2 shows the integrated spectral weights of P3HT polaron absorption peaks based on Equation S3. In Table S2, the relative interchain and intrachain integrations are shown; that is, the values represent the integration of the various absorption peaks for interchain and intrachain components normalized by the sum of both the interchain and intrachain components, as shown in Equations S41 and S42. The A peak was integrated over the range of $\tilde{\nu}$ from 0 cm^{-1} to 1000 cm^{-1}, and the B peak (or P1 peak) was integrated over the range of $\tilde{\nu}$ from 1400 cm^{-1} to 6000 cm^{-1}. The intrachain relative spectral weight is given by:

$$\text{Peak Abs}_i \text{ Relative Intrachain Spectral Weight} = \frac{\Theta_{\text{intra}}^{\text{Abs}_i}}{\Theta_{\text{intra}}^{\text{A Peak}} + \Theta_{\text{inter}}^{\text{A Peak}}} \tag{S41}$$

and the interchain relative spectral weight is given by

$$\text{Peak Abs}_i \text{ Relative Interchain Spectral Weight} = \frac{\Theta_{\text{inter}}^{\text{Abs}_i}}{\Theta_{\text{intra}}^{\text{A Peak}} + \Theta_{\text{inter}}^{\text{A Peak}}} \tag{S42}$$

where $\Theta_{\text{intra or inter}}^{\text{Abs}_i}$ are given in Equation S3. Spectral integration was performed for the experimental data and for the model fits, given as "Experiment" and "Model" in Table S2 respectively.

Table S2: Relative Spectral Weights of Polaron Absorption Peaks

	A Peak (0-1400 cm^{-1})		**P1 or B Peak (1400-6000 cm^{-1})**	
	Intrachain	Interchain	Intrachain	Interchain
Experiment	0.48	0.52	0.74	0.26
Model	0.46	0.54	0.78	0.22

S3.2 UV-Vis and Exciton Absorption Features:

Polarized UV-Vis absorption of solid-state aligned P3HT thin films was performed to assess H- and J-aggregate character of polymer aggregates as measured from exciton absorption features.

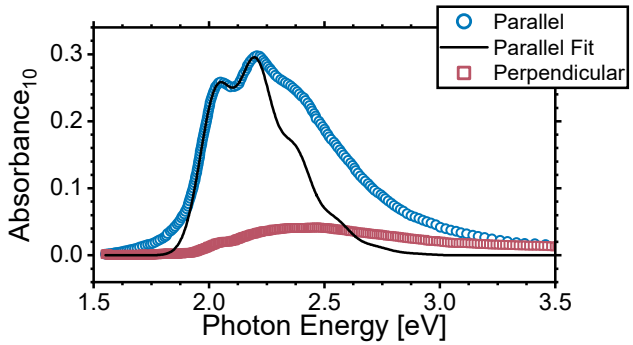

Figure S4: Thin film UV-Vis absorbance for aligned P3HT with incident light polarization aligned parallel and perpendicular to the nominal alignment direction. An H-aggregate vibronic model fit based on Ref. [13] is shown as a solid lines for the parallel alignment directions. An interchain exciton bandwidth of W_{inter} = 36±3 meV was found.

S3.3 X-ray characterization of polymer thin films:

Grazing-incidence X-ray scattering (GIXS) scans of aligned P3HT (Figure S5) display intense scattering peaks associated with a semicrystalline microstructure in OSCs and displays characteristic peaks and spacing associated with P3HT [14, 15, 16]. π-stacking (010) scattering is observed in both the in-plane (Q_{xy}) and out-of-plane (Q_z) directions at Q $= 1.66$ Å^{-1} with a d-spacing of 3.78 Å. Lamellar (100) scattering is also observed in both the Q_{xy} and Q_z directions at Q $= 0.38$ Å^{-1} with a d-spacing of 16.36 Å, though the in-plane lamellar peaks are only observed when the X-ray beam is parallel to the chain alignment as shown in Figure S5. This is indicative of highly-aligned films where the lamellar stacking is expected orthogonal to the chain alignment direction. The inset of Figure S5d shows a shift in the peak at $Q_{xy} \sim 1.65$ Å^{-1}. This shift is likely due to the aligned nature of these P3HT thin films. In uniaxially orientated samples, the in-plane π-stacking is greatly attenuated when the X-ray is aligned perpendicular to the polymer alignment direction (i.e. scattering vector is parallel to the alignment), and a weaker backbone scattering peak at $Q_{xy} \sim 1.52 - 1.56$ Å^{-1} can become more pronounced [14, 15].

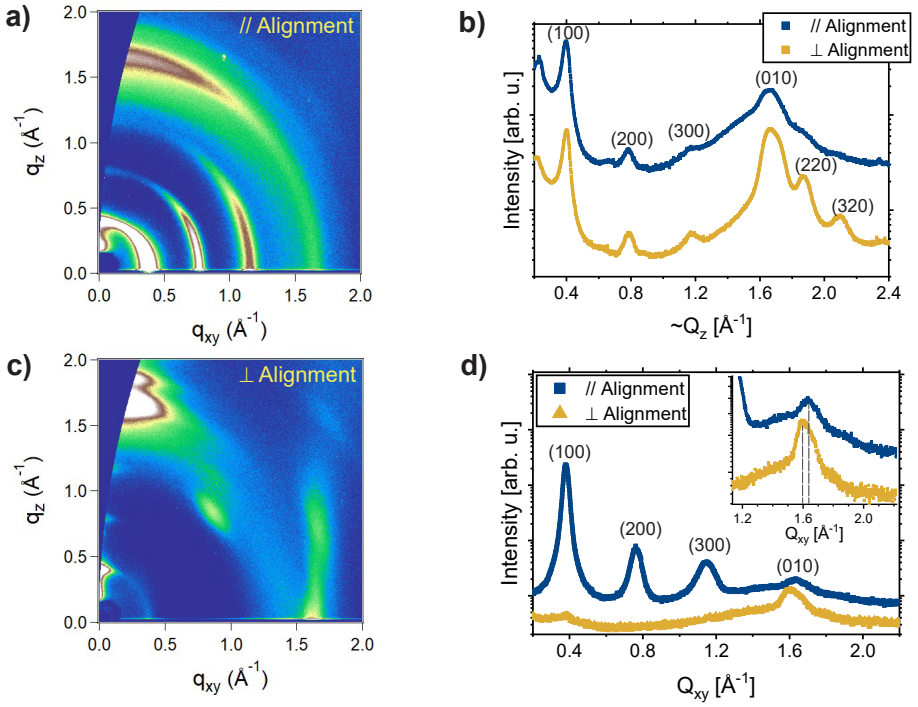

Figure S5: GIXS 2-D images for P3HT with the incident x-ray beam aligned **a)** with the polymer alignment direction, and **c)** aligned perpendicular to the polymer alignment direction. Lineouts for P3HT with the incident X-ray beam aligned **b)** with the polymer alignment direction, and **d)** perpendicular to the polymer alignment direction. Inset shows a slight shift of the scattering peak at $Q_{xy} \sim 1.65$ Å^{-1} between the X-ray beam aligned parallel and perpendicular to the sample. Tentative peak assignments are shown based on previous work [14, 15, 16].

Fits to the in-plane lamellar (100) scattering peak are shown in Figure S6a for the X-ray beam aligned parallel and perpendicular to the polymer alignment direction. Fits were performed with Voigt lineshape functions. The lamellar peak for the case of the X-ray beam aligned perpendicular to the polymer alignment direction is severely reduced compared to the case of the X-ray beam aligned parallel to the polymer chain axis and is scaled by a factor of 100x in Figure S6a. Based off of the fits shown in Figure S6a, there is a ~600 fold difference in the in-plane (100) integrated peak area between the parallel and perpendicular alignment conditions. This again highlights the high degree of uniaxial alignment in these materials, though this will be discussed more quantitatively in Section S3.4.

π-stacking structural coherence and paracrystallinity were estimated based on a Gaussian fit to the in-plane π-stacking peak for the X-ray beam aligned parallel to the polymer alignment direction. The full-width half-maximum

of the π-stacking peak fit ($\Delta Q = 0.086$ Å^{-1}) was used to estimate structural coherence with the Scherrer equation ($l_{c,\pi} = \frac{2\pi K}{\Delta Q} = 65.4$ Å) where K is a shape factor set to 0.9 in this work since the crystalline form is not well defined [17]. The paracrystallinity parameter, g, was estimated using the peak center position ($Q_0 = 1.642$ Å) and the FWHM of the π-stacking peak based on $g = \sqrt{\frac{\Delta Q}{2\pi Q_0}} = \sqrt{\frac{0.086}{2\pi \times 1.64}} = 0.092 = 9.2\%$ [18].

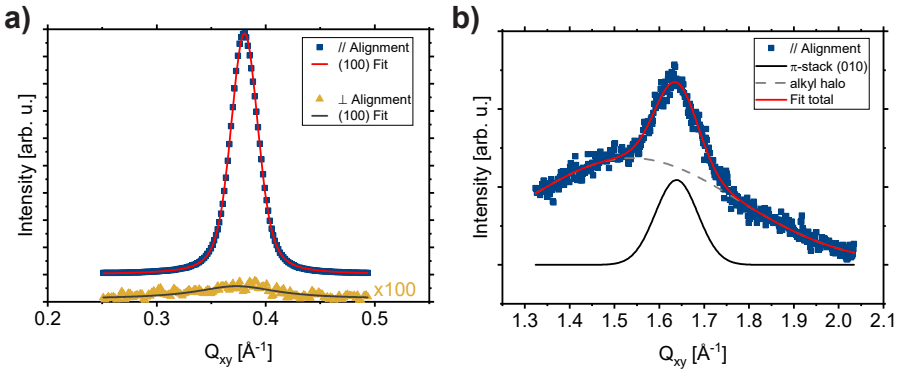

Figure S6: **a)** In-plane GIXS lineouts for the (100) lamellar peak with Voigt peak fits. The relative orientation of the incident X-ray beam relative to the polymer alignment direction is shown in the label. The perpendicular alignment data is multiplied by a factor of 100, and the parallel alignment data is offset vertically for clarity. **b)** In-plane GIXS lineout for the (010) π-stacking peak for the condition of the X-ray beam parallel to the polymer alignment direction. Gaussian peak fits to the broad alkyl halo ~ 1.45 Å^{-1} and the π-stacking peak are shown.

S3.4 Polarized FTIR absorbance:

Figure S7 shows FTIR absorbance spectroscopy that was used to additionally confirm polymer chain alignment. IR absorbance spectroscopy of vibrational modes with TDMs oriented along the polymer backbone, the antisymmetric C=C stretching mode at $\nu_{a,\,\text{C=C}}$=1510 cm^{-1} and the thiophene =C-H stretching mode at $\nu_{\text{=C-H}}$=3050 cm^{-1}, show large dichroic ratios (Table S3) as well as a $\cos^2(\theta)$ dependence on polarization orientation as would be expected for highly oriented polymer backbones (see Equation S27) [19, 20, 21].

Taking the dichroic ratios calculated for the antisymmetric C=C stretching mode at $\nu_{a,\,\text{C=C}}$=1510 cm^{-1} and the thiophene =C-H stretching mode at $\nu_{\text{C-H}}$=3050 cm^{-1}, the uniaxial Hermans orientation factor can be written as a function of absorption dichroic ratio ($D = \text{A}_\parallel/\text{A}_\perp$) and the angle between the absorption transition dipole moment and the polymer chain axis, α, by Equation S43, where $2/(3\cos^2(\alpha) - 1)$ reduces to unity under since $\alpha = 0°$ for the two aforementioned transitions [22, 23, 24]. The reduced D and f for the =C-H mode is likely due to the presence of face-on crystallite populations where the TDM of this vibration is not in the c-axis plane of the polymer. The high D ratios and f values close to unity nevertheless show that polymer chains are well aligned in a uniaxial orientation.

$$f = \frac{D-1}{D+2}\,\frac{2}{3\cos^2(\alpha) - 1} = \frac{D-1}{D+2} \tag{S43}$$

Table S3: Dichroic absorption ratios and Hermans orientation factors of select vibrational modes

Mode	Energy [cm^{-1}]	$D = \text{A}_\parallel/\text{A}_\perp$	f
antisymmetric C=C stretching, $\nu_{a,\,\text{C=C}}$	1510	58	0.95
=C-H stretching $\nu_{\text{C-H}}$	3050	35	0.92

Other vibrational absorption transitions are seen with polarization dependencies in the Figure S7. Most prominently, the transitions between 1400 cm^{-1} and 1480 cm^{-1} display strong polarization dependence. These modes were not analyzed in great detail in this work, as this region comprises both C=C stretching modes along with alkyl side chain CH_2 and CH_3 bending modes. The strong mode at 1449 cm^{-1} seen in 0° spectrum (**E** parallel to chain alignment)

is due to a lower energy C=C stretching mode [21, 25]. As the light polarization moves perpendicular to the chain alignment, this mode decreases in intensity, and a doublet at 1455 cm^{-1} and 1465 cm^{-1} becomes more pronounced, assigned to CH_2 and CH_3 bending modes of the side chains [20, 25]. The mode at 1436 cm^{-1} is of uncertain origin and possibly constitutes a mode associated with C=C stretching similar to that of the mode at 1449 cm^{-1}, but for a different aggregate configuration where the alkyl side chains lie in a different configuration [21].

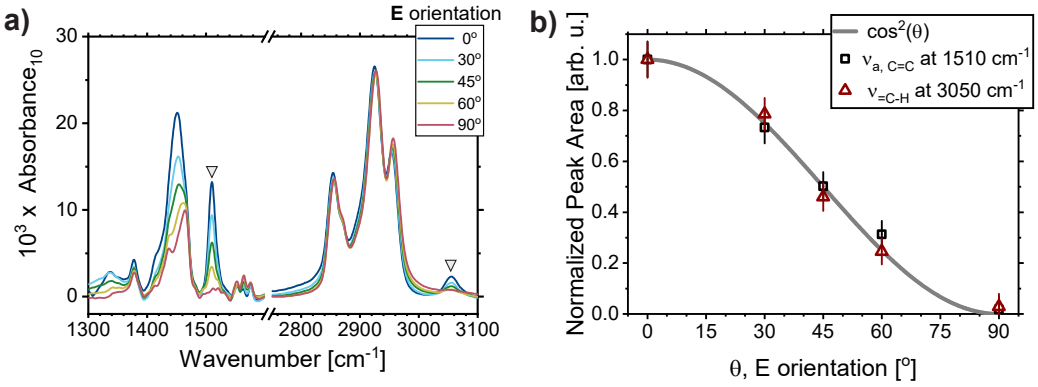

Figure S7: **a)** Polarized IR absorbance collected on aligned P3HT thin films. As in the main text, the **E** orientation refers to the orientation of the electric field vector of the incident light with respect to the c-axis of the polymer chains. Triangle symbols highlight the peaks of interest used to assess polymer in-plane orientation. **b)** Peak areas of the C=C stretching mode at $\nu_{a,\,C=C}$=1510 cm^{-1} and the thiophene =C-H stretching mode at $\nu_{=C\text{-}H}$=3050 cm^{-1} as found from pseudo-voigt fits to the polarized IR absorbance data. Peak areas are normalized to the peak area when the incident light electric field is aligned with the polymer c-axis (i.e. θ=0°). For comparison, the theoretical $\cos^2(\theta)$ dependence expected for polymer films with perfect uniaxial chain orientation is shown as outlined in Equation S23. Error bars represent standard deviation errors propagated from the peak fits as well as the estimated root-mean-squared-error (RMSE) of the FTIR absorbance experiment of $\sim 2 \times 10^{-5}$. RMSE was based on the baseline noise found in the spectral region of $\tilde{\nu}$ from 3100 to 3600 cm^{-1}).

S3.5 Component fits to Polarized CMS Data:

CMS was performed on two samples of aligned P3HT. The aligned P3HT thin films were prepared on separate Silicon substrates at the same time, but then CMS sample electrical contact preparation and CMS measurements (see S1.6) were finished for the two aligned P3HT samples at two separate times approximately 21 days apart. The two separate samples were aligned orthogonal in the FTIR spectrometer. Sample 1 was aligned with the sample X-direction (polymer c-axis) along the spectrometer out-of-plane direction, and Sample 2 was aligned with the sample X-direction along the spectrometer in-plane direction. This was done to ensure that CMS data was reproducible and not susceptible to possible inherent polarization arising from infrared focusing optics and detectors in the FTIR spectrometer. Sample 2 had a higher $\Delta T/T$ signal ($\sim 15\%$) compared to Sample 1. We suspect the difference arises from possible differences in sample alignment to the infrared light focus and sample overlap with the infrared light spot. CMS samples have semi-transparent gold electrical contacts on the polymer thin-films that do not cover the entire polymer surface, so an infrared light focus that overlaps the semi-transparent contact more will have more sample undergoing charge modulation and thus a greater $\Delta T/T$ signal. Nevertheless, the trend between the two samples is remarkably consistent as shown in Figure S8, and the presence of a substantial *intrachain* component at low energies ($\tilde{\nu} < 1400$ cm^{-1}) is clear and consistent across both samples tested.

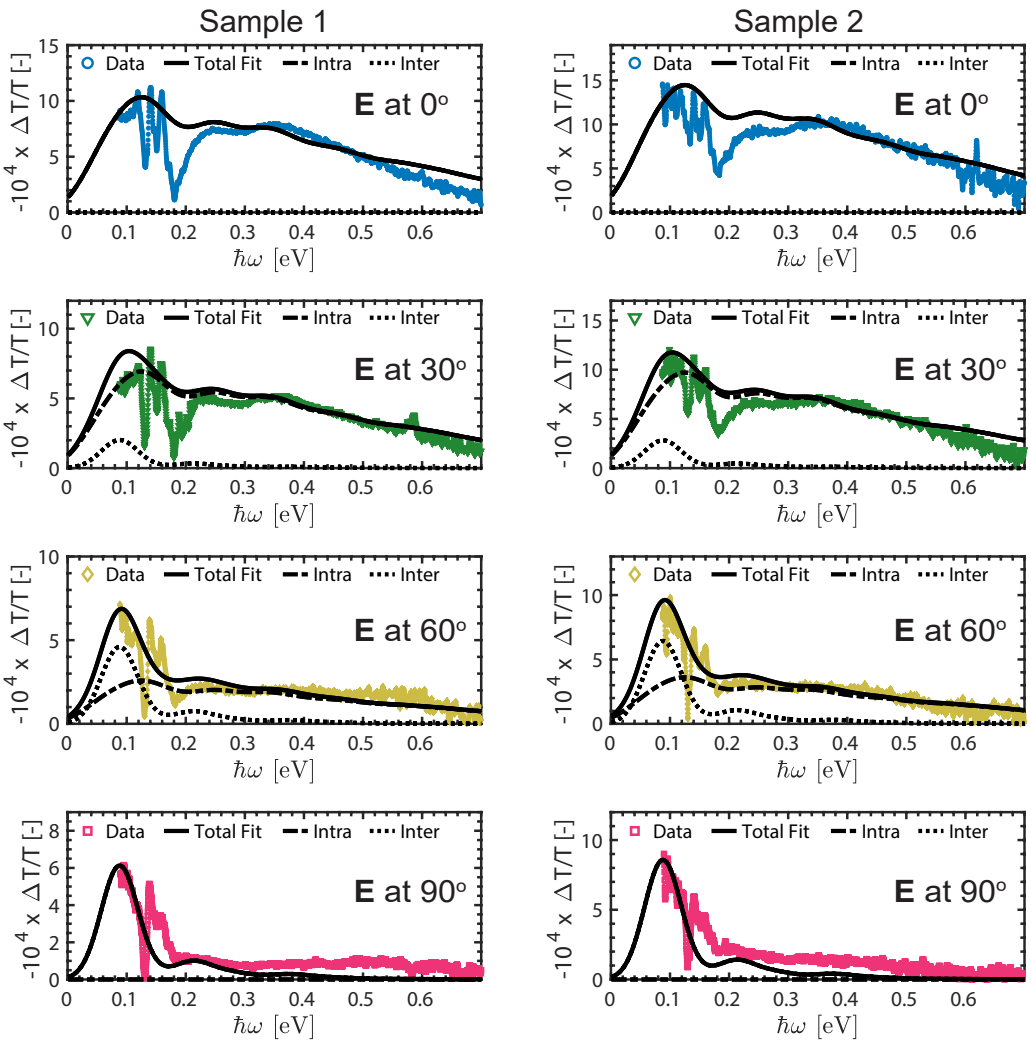

Figure S8: Model fit components for two separately prepared samples with various electric field, **E**, orientations. Raw $\Delta T/T$ data (symbols) are shown alongside total model fits (solid lines) with the comprising intrachain and interchain components shown separately as "Intra" and "Inter" respectively. The total model fit ("Total Fit") is the sum of intrachain and interchain components, and the components are scaled according to Equations S27 and S28. Again, we emphasize that this scaling of the two components is entirely consistent with the measured out-of-plane crystallite orientation and is not arbitrary or independent between the inter- and intrachain model components. Note that the ordinate scale is adjusted between panels to highlight the individual fits.

S3.6 Effect of vibronic coupling on polaron absorption spectra

Figure S9 demonstrates the importance of vibronic coupling on the mid-IR polaron absorption line shape. The simulated absorption spectra with and without vibronic coupling are shown for various M monomer x N chain π-stacks. The spectra without vibronic coupling are evaluated by removing the third and fourth terms in the Hamiltonian in Equation 4 of the main text (H_0) (i.e. removing $\hbar\omega_{\text{vib}}\sum_{m=1}^{M}\sum_{n=1}^{N} b_{m,n}^{\dagger}b_{m,n}$ and $\hbar\omega_{\text{vib}}\sum_{m=1}^{M}\sum_{n=1}^{N}\left(\lambda(b_{m,n}^{\dagger}+b_{m,n})+\lambda^2\right)d_{m,n}^{\dagger}d_{m,n}$)). If the vibronic coupling is included, as is done in the main text, the spectrum separates into peaks **A** and **B**. This effect is more pronounced as the polaron localizes, as is accomplished in Figure S9 by reducing the aggregate dimensions. Spectral line shapes with clear **A** and **B** structure depicting more localized polarons are well documented in the literature for doped P3HT films, where localization is accomplished by Coulomb binding to the dopant anion [26, 27, 28, 29]. In the absence of vibronic coupling (right panel Figure S9) there is no distinct separation of peak **A** and peak **B**. The inset of Figure S9 also shows a qualitative energy level scheme for the polaron transitions

expected under strong polaron localization, where the Herzberg-Teller mechanism is operative [26, 27, 30]. It should be emphasized that neglecting vibronic coupling in the model employed here (right panel of Figure S9) still leads to a different picture than the adiabatic interpretation of mid-gap states shown in Figure 1 of the main text.

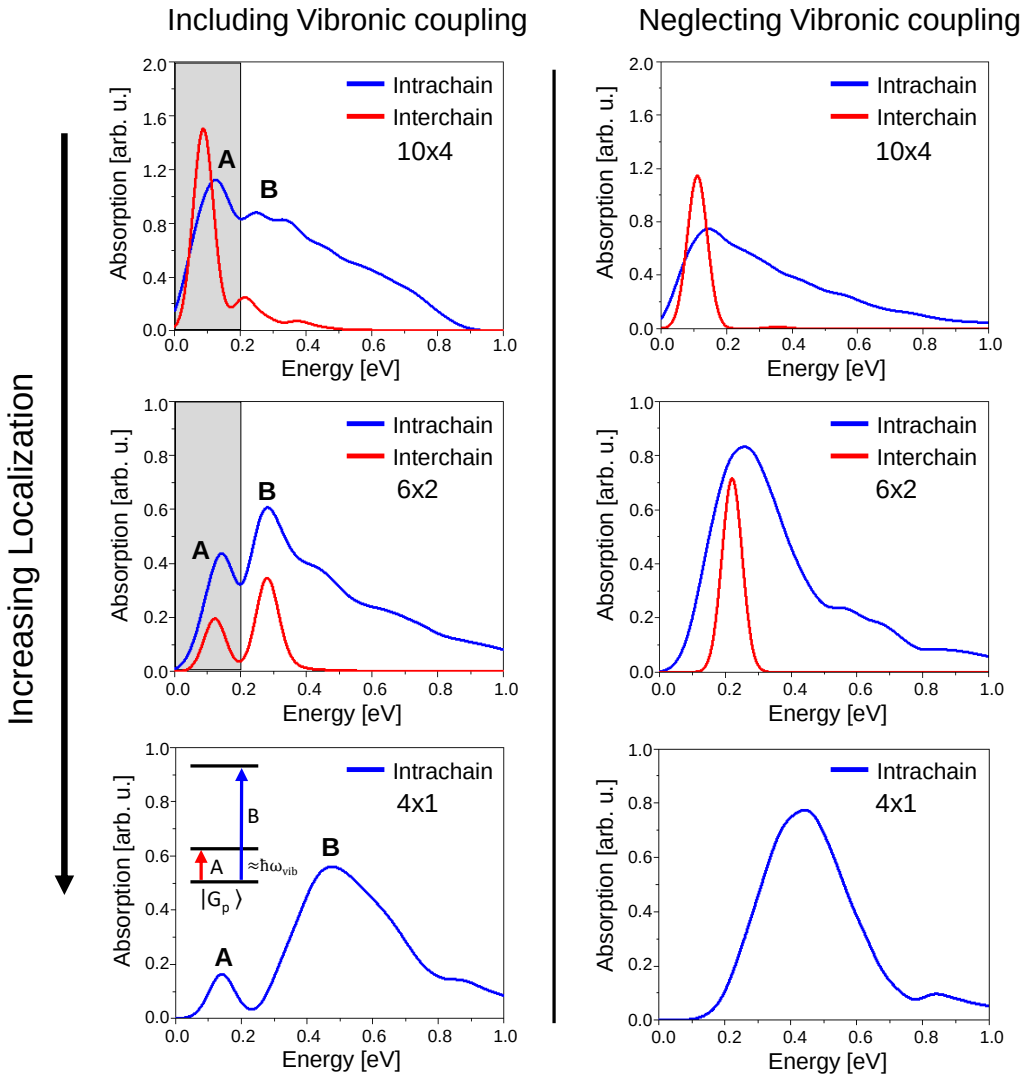

Figure S9: Simulated mid-infrared polaron absorption spectrum with vibronic coupling included (left panels) and with vibronic coupling removed (right panel) as a function of decreasing lattice size as shown in the inset labels (labeled as M monomers $\times$ N chains). The left panel shows the demarcation of peak **A** and peak **B** upon activation of vibronic coupling. The spectral region of peak **A** is highlighted in the 10x4 and 6x2 stacks to show that peak **A** arises from both the intra- and interchain components. The addition of vibronic coupling creates two separate peaks that match closely with the experimental data shown in Figure 4 of the main text and Figure S8. The remaining parameters defining the Hamiltonian are identical as shown in Table S1 with t_{intra} = -0.4 eV, t_{inter} = -0.11 eV and σ_{dis} = 0.3 eV. 5000 disorder configurations were done to obtain converged absorption spectra. In the bottom left panel, a qualitative energy level schematic is shown for the transitions that lead to peak **A** and peak **B**. , based on the explanations in Refs. [27] and [30]. $|G_p\rangle$ represents the hole polaron ground state, and $\hbar\omega_{\text{vib}}$ is the aromatic-quinoidal stretching mode at 0.17 eV.

References

[1] Amer Hamidi-Sakr et al. "A Versatile Method to Fabricate Highly In-Plane Aligned Conducting Polymer Films with Anisotropic Charge Transport and Thermoelectric Properties: The Key Role of Alkyl Side Chain Layers on the Doping Mechanism". In: *Advanced Functional Materials* 27.25 (2017), p. 1700173. ISSN: 1616-301X. DOI: 10.1002/adfm.201700173. URL: https://dx.doi.org/10.1002/adfm.201700173.

[2] Jan Ilavsky. "Nika: software for two-dimensional data reduction". In: *Journal of Applied Crystallography* 45.2 (2012), pp. 324–328. ISSN: 0021-8898. DOI: 10.1107/s0021889812004037.

[3] Stefan D. Oosterhout et al. "Mixing Behavior in Small Molecule:Fullerene Organic Photovoltaics". In: *Chemistry of Materials* 29.7 (2017), pp. 3062–3069. ISSN: 0897-4756. DOI: 10.1021/acs.chemmater.7b00067. URL: https://dx.doi.org/10.1021/acs.chemmater.7b00067.

[4] Robert H. Norton and Reinhard Beer. "New apodizing functions for Fourier spectrometry". In: *Journal of the Optical Society of America* 66.3 (1976), pp. 259–264. DOI: 10.1364/JOSA.66.000259. URL: https://opg.optica.org/abstract.cfm?URI=josa-66-3-259.

[5] L. Mertz. "Auxiliary computation for Fourier spectrometry". In: *Infrared Physics* 7.1 (1967), pp. 17–23. ISSN: 0020-0891. DOI: https://doi.org/10.1016/0020-0891(67)90026-7. URL: https://www.sciencedirect.com/science/article/pii/0020089167900267.

[6] Jessy L. Baker et al. "Quantification of Thin Film Crystallographic Orientation Using X-ray Diffraction with an Area Detector". In: *Langmuir* 26.11 (2010), pp. 9146–9151. ISSN: 0743-7463. DOI: 10.1021/la904840q. URL: https://dx.doi.org/10.1021/la904840q.

[7] Michael L. Chabinyc et al. "X-ray Scattering Study of Thin Films of Poly(2,5-bis(3-alkylthiophen-2-yl)thieno[3,2-b]thiophene)". In: *Journal of the American Chemical Society* 129.11 (2007), pp. 3226–3237. ISSN: 0002-7863. DOI: 10.1021/ja0670714. URL: https://dx.doi.org/10.1021/ja0670714.

[8] Christopher M. Pochas and Frank C. Spano. "New insights on the nature of two-dimensional polarons in semiconducting polymers: Infrared absorption in poly(3-hexylthiophene)". In: *The Journal of Chemical Physics* 140.24 (2014), p. 244902. ISSN: 0021-9606. DOI: 10.1063/1.4882696. URL: https://dx.doi.org/10.1063/1.4882696.

[9] Raja Ghosh, Christopher M. Pochas, and Frank C. Spano. "Polaron Delocalization in Conjugated Polymer Films". In: *The Journal of Physical Chemistry C* 120.21 (2016), pp. 11394–11406. ISSN: 1932-7447. DOI: 10.1021/acs.jpcc.6b02917. URL: https://dx.doi.org/10.1021/acs.jpcc.6b02917.

[10] Scott Himmelberger et al. "Role of Side-Chain Branching on Thin-Film Structure and Electronic Properties of Polythiophenes". In: *Advanced Functional Materials* 25.17 (2015), pp. 2616–2624. ISSN: 1616301X. DOI: 10.1002/adfm.201500101.

[11] Manabu Kiguchi et al. "Accumulation and Depletion Layer Thicknesses in Organic Field Effect Transistors". In: *Japanese Journal of Applied Physics* 42.Part 2, No. 12A (2003), pp. L1408–L1410. ISSN: 0021-4922. DOI: 10.1143/jjap.42.l1408. URL: https://dx.doi.org/10.1143/jjap.42.l1408.

[12] R. A. Street, J. E. Northrup, and A. Salleo. "Transport in polycrystalline polymer thin-film transistors". In: *Physical Review B* 71.16 (2005). ISSN: 1098-0121. DOI: 10.1103/physrevb.71.165202. URL: https://dx.doi.org/10.1103/physrevb.71.165202.

[13] Jenny Clark et al. "Determining exciton bandwidth and film microstructure in polythiophene films using linear absorption spectroscopy". In: *Applied Physics Letters* 94.16 (2009), p. 163306. ISSN: 0003-6951. DOI: 10.1063/1.3110904. URL: https://dx.doi.org/10.1063/1.3110904.

[14] Leslie H. Jimison et al. "Charge-Transport Anisotropy Due to Grain Boundaries in Directionally Crystallized Thin Films of Regioregular Poly(3-hexylthiophene)". In: *Advanced Materials* 21.16 (2009), pp. 1568–1572. ISSN: 0935-9648. DOI: 10.1002/adma.200802722. URL: https://dx.doi.org/10.1002/adma.200802722.

[15] Brendan O'Connor et al. "Anisotropic Structure and Charge Transport in Highly Strain-Aligned Regioregular Poly(3-hexylthiophene)". In: *Advanced Functional Materials* 21.19 (2011), pp. 3697–3705. ISSN: 1616-301X. DOI: 10.1002/adfm.201100904. URL: https://dx.doi.org/10.1002/adfm.201100904.

[16] Christian Müller et al. “One-Step Macroscopic Alignment of Conjugated Polymer Systems by Epitaxial Crystallization during Spin-Coating”. In: *Advanced Functional Materials* 23.19 (2013), pp. 2368–2377. ISSN: 1616-301X. DOI: 10.1002/adfm.201202983. URL: https://dx.doi.org/10.1002/adfm.201202983.

[17] Zhengxing Peng, Long Ye, and Harald Ade. “Understanding, quantifying, and controlling the molecular ordering of semiconducting polymers: from novices to experts and amorphous to perfect crystals”. In: *Materials Horizons* 9.2 (2022), pp. 577–606. ISSN: 2051-6347. DOI: 10.1039/d0mh00837k. URL: https://dx.doi.org/10.1039/d0mh00837k.

[18] Jonathan Rivnay et al. “Structural origin of gap states in semicrystalline polymers and the implications for charge transport”. In: *Physical Review B* 83.12 (2011). ISSN: 1098-0121. DOI: 10.1103/physrevb.83.121306. URL: https://dx.doi.org/10.1103/PhysRevB.83.121306.

[19] Marc C. Gurau et al. “Measuring Molecular Order in Poly(3-alkylthiophene) Thin Films with Polarizing Spectroscopies”. In: *Langmuir* 23.2 (2007), pp. 834–842. ISSN: 0743-7463. DOI: 10.1021/la0618972. URL: https://dx.doi.org/10.1021/la0618972.

[20] Luigi Brambilla et al. “Regio-Regular Oligo and Poly(3-hexyl thiophene): Precise Structural Markers from the Vibrational Spectra of Oligomer Single Crystals”. In: *Macromolecules* 47.19 (2014), pp. 6730–6739. ISSN: 0024-9297. DOI: 10.1021/ma501614c. URL: https://dx.doi.org/10.1021/ma501614c.

[21] L. Brambilla et al. “Infrared and multi-wavelength Raman spectroscopy of regio-regular P3HT and its deutero derivatives”. In: *Journal of Raman Spectroscopy* 49.3 (2018), pp. 569–580. ISSN: 0377-0486. DOI: 10.1002/jrs.5301. URL: https://dx.doi.org/10.1002/jrs.5301.

[22] Gabriel Guenoun et al. “Crystalline orientation assessment in transversely isotropic semicrystalline polymer: Application to oedometric compaction of PTFE”. In: *Polymer Engineering and Science* 61.1 (2021), pp. 107–114. ISSN: 0032-3888. DOI: 10.1002/pen.25561. URL: https://dx.doi.org/10.1002/pen.25561.

[23] James L. White and Joseph E. Spruiell. “The specification of orientation and its development in polymer processing”. In: *Polymer Engineering and Science* 23.5 (1983), pp. 247–256. ISSN: 0032-3888. DOI: 10.1002/pen.760230503. URL: https://dx.doi.org/10.1002/pen.760230503.

[24] K. C. Cole et al. “A new approach to the characterization of molecular orientation in uniaxially and biaxially oriented samples of poly(ethylene terephthalate)”. In: *Polymer* 40.12 (1999), pp. 3505–3513. ISSN: 00323861. DOI: 10.1016/s0032-3861(98)00574-6.

[25] Guy Louarn et al. “Raman Spectroscopic Studies of Regioregular Poly(3-alkylthiophenes)”. In: *The Journal of Physical Chemistry* 100.30 (1996), pp. 12532–12539. ISSN: 0022-3654. DOI: 10.1021/jp960104p. URL: https://dx.doi.org/10.1021/jp960104p.

[26] Raja Ghosh et al. “Spectral Signatures and Spatial Coherence of Bound and Unbound Polarons in P3HT Films: Theory Versus Experiment”. In: *The Journal of Physical Chemistry C* 122.31 (2018), pp. 18048–18060. ISSN: 1932-7447. DOI: 10.1021/acs.jpcc.8b03873. URL: https://dx.doi.org/10.1021/acs.jpcc.8b03873.

[27] Raja Ghosh et al. “Anisotropic Polaron Delocalization in Conjugated Homopolymers and Donor–Acceptor Copolymers”. In: *Chemistry of Materials* (2019). ISSN: 0897-4756. DOI: 10.1021/acs.chemmater.9b01704. URL: https://dx.doi.org/10.1021/acs.chemmater.9b01704.

[28] D. Tyler Scholes et al. “The Effects of Crystallinity on Charge Transport and the Structure of Sequentially Processed F ₄ TCNQ-Doped Conjugated Polymer Films”. In: *Advanced Functional Materials* 27.44 (2017), p. 1702654. ISSN: 1616-301X. DOI: 10.1002/adfm.201702654. URL: https://dx.doi.org/10.1002/adfm.201702654.

[29] Taylor J. Aubry et al. “Tunable Dopants with Intrinsic Counterion Separation Reveal the Effects of Electron Affinity on Dopant Intercalation and Free Carrier Production in Sequentially Doped Conjugated Polymer Films”. In: *Advanced Functional Materials* 30.28 (2020), p. 2001800. ISSN: 1616-301X. DOI: 10.1002/adfm.202001800. URL: https://dx.doi.org/10.1002/adfm.202001800.

[30] Raja Ghosh and Frank C. Spano. “Excitons and Polarons in Organic Materials”. In: *Accounts of Chemical Research* 53.10 (2020), pp. 2201–2211. ISSN: 0001-4842. DOI: 10.1021/acs.accounts.0c00349. URL: https://dx.doi.org/10.1021/acs.accounts.0c00349.